nature communications

Article

https://doi.org/10.1038/s41467-024-55041-z

Topological transformation of microbial proteins into iron single-atom sites for selective hydrogen peroxide electrosynthesis

Received: 25 March 2024

Accepted: 29 November 2024

Published online: 30 December 2024

Check for updates

Xiaofeng Xiao[1,2,9], Zechao Zhuang[3,4,9], Shuhu Yin[5], Jiexin Zhu[6], Tao Gan[7], Ruohan Yu[8], Jinsong Wu[8], Xiaochun Tian[1], Yanxia Jiang[5], Dingsheng Wang[3] ✉ & Feng Zhao[1] ✉

The emergence of single-atom catalysts offers exciting prospects for the green production of hydrogen peroxide; however, their optimal local structure and the underlying structure–activity relationships remain unclear. Here we show trace Fe, up to 278 mg/kg and derived from microbial protein, serve as precursors to synthesize a variety of Fe single-atom catalysts containing $FeN_{5-x}O_x$ ($1 \le x \le 4$) moieties through controlled pyrolysis. These moieties resemble the structural features of nonheme Fe-dependent enzymes while being effectively confined on a microbe-derived, electrically conductive carbon support, enabling high-current density electrolysis. A comparative analysis involving catalysts derived from eleven representative microbes reveals that the presence of 0.05 wt% Fe single-atom sites leads to a significant 26% increase in hydrogen peroxide selectivity. Remarkably, the optimal catalyst featuring FeN_3O_2 sites demonstrates a selectivity of up to 93.7% and generates hydrogen peroxide in a flow cell at an impressive rate of 29.6 mol g^{-1} h^{-1} at 200 mA cm^{-2}. This work achieves structural fine-tuning of metal single-atom sites at the trace level and provides topological insights into single-atom catalyst design to achieve cost-efficient hydrogen peroxide production.

Hydrogen peroxide (H_2O_2) is highly valuable in various chemical, pharmaceutical, and environmental applications[1,2]. However, the current primary method for H_2O_2 production relies on an energy-intensive anthraquinone-based process[3]. A cleaner and more electrified alternative is clearly needed to achieve sustainability[4]. The electrochemical synthesis of H_2O_2 via the two-electron ($2e^-$) oxygen reduction reaction (ORR) provides more possibilities for decentralized onsite production, which effectively mitigates production costs, transportation expenses, and safety risks[5,6].

Single-atom catalysts (SACs) are cutting-edge electrocatalysts that enable cost-effective electrochemical production of H_2O_2, demonstrating superior catalytic activity and target product selectivity

[1]Key Laboratory of Urban Pollutant Conversion, Institute of Urban Environment, Chinese Academy of Sciences, Xiamen, China. [2]University of Chinese Academy of Sciences, Beijing, China. [3]Department of Chemistry, Tsinghua University, Beijing, China. [4]Department of Chemical Engineering, Columbia University, New York, NY, USA. [5]College of Chemistry and Chemical Engineering, Discipline of Intelligent Instrument and Equipment, Xiamen University, Xiamen, China. [6]State Key Laboratory of Advanced Technology for Materials Synthesis and Processing, Wuhan University of Technology, Wuhan, China. [7]Shanghai Synchrotron Radiation Facility, Shanghai Advanced Research Institute, Chinese Academy of Sciences, Shanghai, China. [8]Nanostructure Research Centre, Wuhan University of Technology, Wuhan, China. [9]These authors contributed equally: Xiaofeng Xiao, Zechao Zhuang.
✉e-mail: wangdingsheng@mail.tsinghua.edu.cn; fzhao@iue.ac.cn

in the 2e⁻ ORR[7–10]. Despite their ultralow active site loading, SACs exhibit notable performance[11]. These trace single-atom sites, often found in heteroatom-doped carbon materials, form spontaneously during pyrolysis and work synergistically with nonmetallic doping sites[12,13]. The use of microbes as precursors facilitates the scalable gram-level synthesis of heteroatom-doped carbon materials, bridging the gap between lab-scale advancements and industrial applications[14]. In microbial precursors, trace amounts of iron (Fe) act as metalloprotein centres confined by protein ligands with well-defined stereoconfigurations, providing an ideal framework for the formation of Fe single-atom sites. While these trace Fe single-atom sites significantly contribute to ORR performance, the optimal local structure and the underlying structure–activity relationships remain unclear[15,16]. This lack of information is particularly evident for the active site H_2O_2 production, as Fe SACs are traditionally predisposed to reducing O_2 to H_2O via haem sites (FeN_4 moiety). However, Fe SACs possess a moderate O_2 binding affinity, allowing them to readily convert between various Fe–O intermediates[17–20]. By fine-tuning the coordination environment of Fe SACs, the selective conversion of different ORR products can be achieved[21–23]. When Fe SACs mimic the distinct metal environment of superoxide dismutase and superoxide reductase, they are endowed with the ability to undergo oxidative metabolism and protect against reactive oxygen species[24–27]. Their nonheme configurations, characterized by distorted square pyramidal geometries and electronic asymmetry, provide the structural basis for the selective reduction of Fe–O intermediates to H_2O_2[28,29]. Mimicking these natural nonheme Fe-dependent enzymes or inheriting their characteristics at the atomic level[30] is essential for unlocking their full potential for sustainable H_2O_2 production.

Designing multiple tailored active sites, especially those that transform metalloproteins into single-atom sites, is crucial for optimizing the performance of biomass-derived carbon materials. Here, we exploit thermally induced topological transformations of microbial Fe-dependent proteins to synthesize a series of Fe active sites, comprising $FeN_{5-x}O_x$ ($1 \le x \le 4$) moieties, for efficient 2e⁻ ORR. Upon heating, structural changes occur around the Fe species within the protein. The application of heat at different temperatures affects the degree of protein dehydration, deamination, and/or decarboxylation, resulting in various coordination environments of Fe SACs. This process allows continuous modulation of the N/O coordination ratio in $FeN_{5-x}O_x$ moieties to optimize catalyst performance while providing insights into the structure–performance relationship by evaluating the catalyst series. Notably, the optimal catalyst, featuring FeN_3O_2 sites, demonstrated a selectivity of up to 93.7% and produced H_2O_2 in a flow cell at a high rate of 29.6 mol g^{-1} h^{-1} under a current density of 200 mA cm^{-2}. Our computational analysis further revealed the significance of axial oxygen in FeN_3O_2 during the 2e⁻ORR. This work achieves structural fine-tuning of metal single-atom sites at the trace level and provides topological insights into SAC design to achieve cost-efficient H_2O_2 production.

Results

Prevalence of SACs transformed from microbial metalloproteins

Microorganisms undergo pyrolysis to yield porous carbon-based materials that serve as effective ORR electrocatalysts. Eleven species of microorganisms commonly employed in both industrial bioproduction[31] and scientific research[32] were selected as pyrolysis precursors to obtain a comprehensive understanding of microbe-derived carbon materials. The microbial information and cultivation conditions are shown in Supplementary Table 1. The selected species included one eukaryotic strain and ten bacterial strains, representing diverse biological classifications, as depicted in Fig. 1a. The ten bacterial strains belong to the Proteobacteria and Firmicutes phyla, which are among the most common bacterial domains and include seven genera. Pairwise comparisons were performed to determine the genetic distances and assess the genetic diversity among these strains. The results of these comparisons are presented in Fig. 1b and Supplementary Table 2. The greater the genetic distance of pairwise comparisons is, the more significant the difference in genetic information. Among the selected microorganisms, *Bacillus thuringiensis*, *Bacillus subtilis* and *Bacillus pumilus* belong to the same genus, *Bacillus*. *Escherichia coli*, *Shewanella oneidensis*, *Halomonas titanicae*, *Pseudomonas aeruginosa*, *Cupriavidus necator*, *Eubacterium limosum*, *Lactobacillus acidophilus* and *Saccharomyces cerevisiae* are not closely related to the *Bacillus* genus in terms of biological affinity. Thus, these species can serve as representative examples of common microbial strains used for the preparation of microbe-derived carbon materials.

In microbe-derived carbon materials, both the content and the intrinsic activity of atomically dispersed metal sites are key factors determining differences in catalytic performance in the ORR. A rotating ring-disk electrode was used to test the ORR catalytic performance, and its collection efficiency was calibrated, as shown in Supplementary Fig. 1. The selected microorganisms were pyrolysed at 600 °C, resulting in ORR catalysts that predominantly catalysed the reaction via the 2e⁻ pathway. A summary of their catalytic performance is presented in Supplementary Fig. 2 and Fig. 1c. With the exception of the notably inferior performance of the *Lactobacillus acidophilus*-derived carbon material, the remaining ten materials presented half-wave potentials ranging from 0.65 to 0.67 V *vs.* RHE and H_2O_2 selectivities ranging from 77.8% to 93.7%. Among them, the *Bacillus pumilus*-derived carbon material exhibited the optimal ORR activity and H_2O_2 selectivity. Compared with the *Lactobacillus acidophilus*-derived carbon material, the *Bacillus pumilus*-derived carbon material presented a positive shift of 0.1 V in the half-wave potential, reaching 0.65 V *vs.* RHE, and increased selectivity by 28.8% H_2O_2 at 0.6 V *vs.* RHE, reaching 93.7%. H_2O_2 selectivity was correlated with the metal content to explore whether these differences in ORR performance were induced by atomically dispersed metal sites. The H_2O_2 selectivities at 0.6 V *vs.* RHE are plotted against the contents of metal elements in microbe-derived carbon materials in Fig. 1d, including magnesium (Mg), manganese (Mn), Fe, zinc (Zn), copper (Cu), nickel (Ni) and cobalt (Co). The corresponding contents of each strain are presented in Supplementary Fig. 3. Specifically, in the case of the *Lactobacillus acidophilus*-derived carbon material, the contents of Mg and Fe were lower, whereas the content of Mn was significantly higher. Aside from the three metal elements that exhibited distinct variations, the contents of the remaining elements closely resembled those found in other microbe-derived carbon materials.

While Mg, Fe and Mn have been identified as possible influencing elements, determining whether they produce reactive atomic sites is still crucial. According to the elemental distribution of microbe-derived carbon materials (Supplementary Figs. 4–14), Mg tended to agglomerate and form nanoparticles, whereas Mn, Fe, Zn, Cu, Ni, and Co tended to disperse atomically. A sufficient number of highly active single-atom site must be formed using metal elements to improve the ORR catalytic performance. Mn, which had a content similar to that of Fe, is more likely to form 4-electron catalytic sites[33,34]. The Zn content was lower than that of Fe, whereas the contents of Cu, Ni, and Co were one to two orders of magnitude lower. Therefore, compared with other metal sites, Fe single-atom sites may have a greater impact on the catalytic performance of microbe-derived carbon materials. Fe is an abundant element on Earth and a biologically essential component of nearly all living organisms. Notably, *Lactobacillus acidophilus* is a lactic acid bacterium with unique metabolic characteristics that do not depend on Fe[35], resulting in significantly lower iron contents in both *Lactobacillus acidophilus* and its derived carbon material. A horizontal comparison of the eleven microbe-derived carbon materials suggested that trace amounts of Fe may impact their ORR performance.

A vertical comparison of microbe-derived carbon materials was conducted to determine whether Fe-dependent proteins were

https://doi.org/10.1038/s41467-024-55041-z

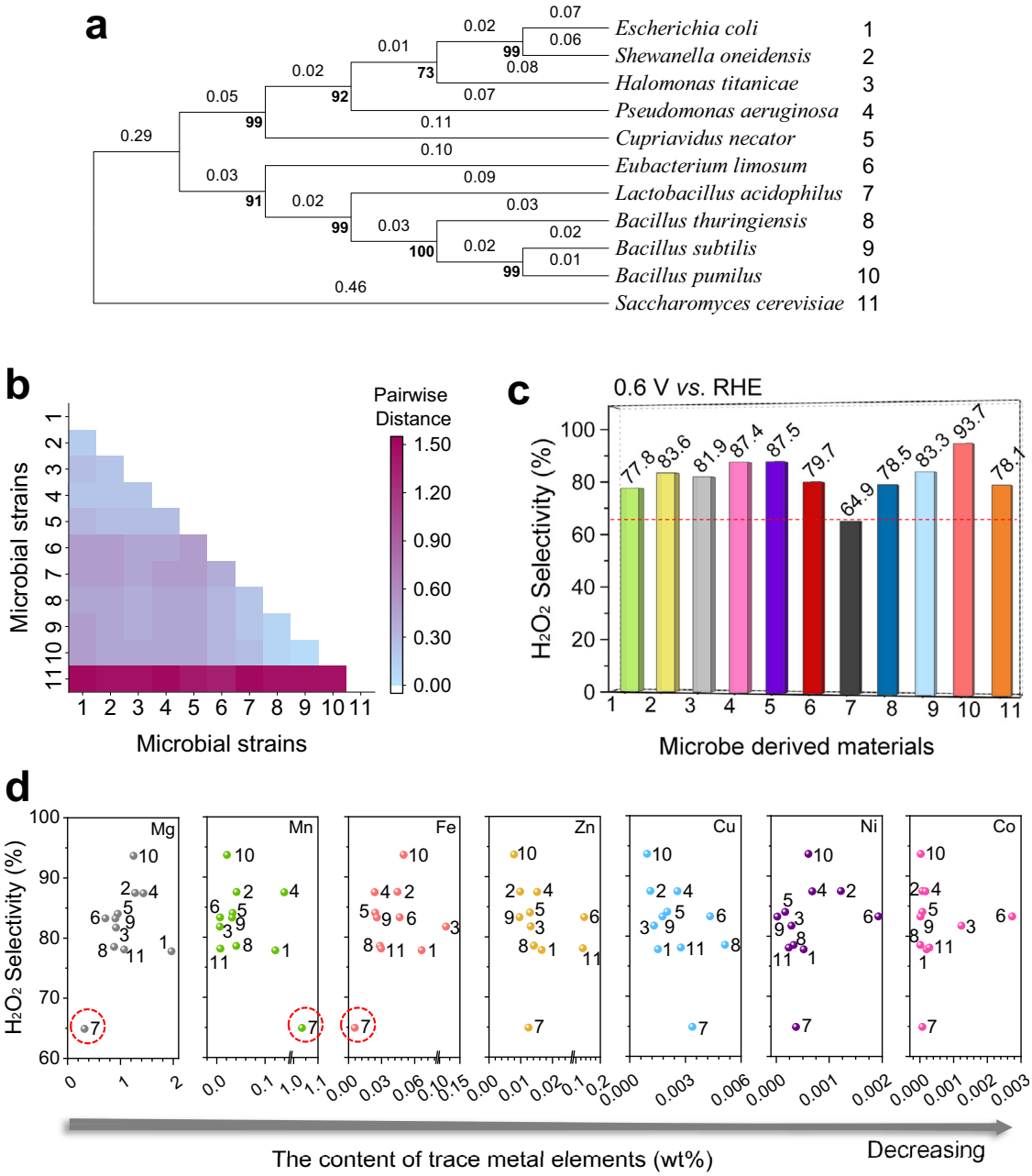

Fig. 1 | Evaluation of microbe-derived electrocatalysts for H_2O_2 production. **a** Molecular phylogenetic analysis of 16S (and 18S of *Saccharomyces cerevisiae*) rRNA gene sequences using the maximum likelihood method. **b** Genetic distances of amino acid sequences determined using the Poisson correction model. **c** H_2O_2 selectivity of various microbe-derived electrocatalysts. **d**, Relationships between the contents of metal elements in microbe-derived electrocatalysts and their H_2O_2 selectivity. The numerical ordinal numbers accompanying the strain names in (**a**) correspond to the microbial strains and their derived carbon materials in (**b**, **d**), respectively. During the electrochemical measurements, 85% iR compensation was applied.

transformed into active Fe sites for H_2O_2 production. *Bacillus pumilus*, which was selected for its superior catalytic performance among microbe-derived carbon materials, was investigated in detail. This robust probiotic strain, which is commonly sourced from chassis cells utilized in industrial biochemical production[36], expresses a variety of Fe-dependent proteins[37], including ferredoxin, cytochrome *c* oxidase, and Fe-dependent superoxide dismutase. The expression of these proteins is closely linked to the metabolic regulation of this microorganism, which enables the tailored cultivation of microbial strains with reduced iron–protein contents for comparative studies. After four iterative cultures in customized iron-free media (see Supplementary Table 1), *Bacillus pumilus* was transformed into a mutant strain, designated *Bacillus pumilus*(Fe−), as shown schematically in Fig. 2a. The cellular structures of *Bacillus pumilus* and *Bacillus pumilus*(Fe−) are essentially indistinguishable under an electron microscope, as shown in Supplementary Fig. 15. However, *Bacillus pumilus*(Fe−) presented a markedly reduced iron content, with an approximately 72% decrease, as shown in Supplementary Fig. 16. During cultivation in the absence of iron sources, *Bacillus pumilus*(Fe−) compensated by assimilating other metal ions, which were used to express proteins that substitute for the deficient Fe-dependent proteins[37,38]. Consequently, the contents of Mg, Mn and Zn in *Bacillus pumilus*(Fe−) increased by 2.2, 6.6, and 0.1 times, respectively.

Bacillus pumilus(Fe−) cells were processed into the *Bacillus pumilus*(Fe−)-derived carbon material, which functioned as a comparative catalyst in contrast to the *Bacillus pumilus*-derived carbon

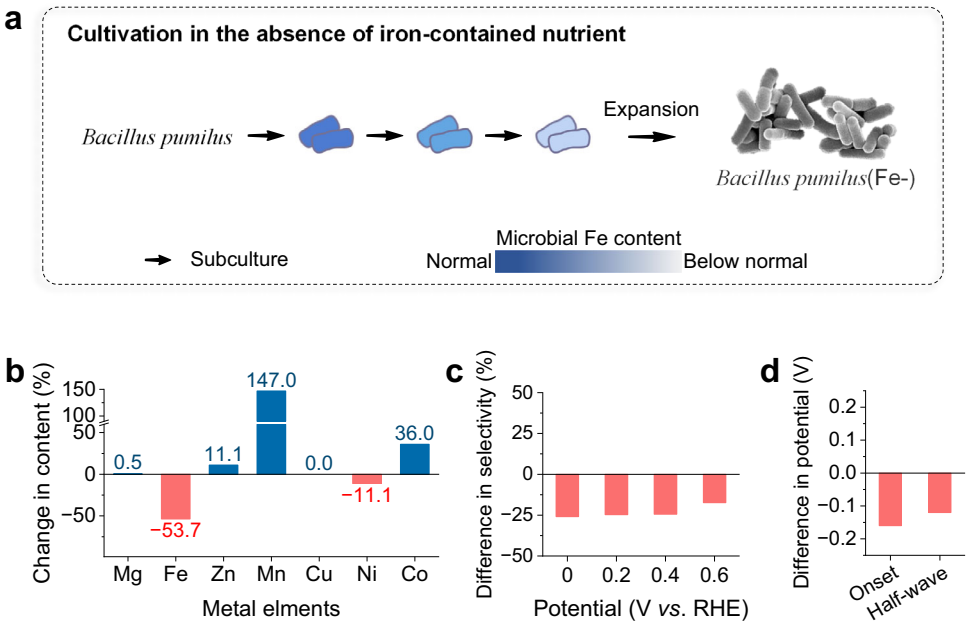

Fig. 2 | Effects of trace Fe sites on the *Bacillus pumilus*-derived carbon material. **a** Schematic of the preparation of microbial treatment samples of *Bacillus pumilus*(Fe−). **b** Changes in the metal content between the *Bacillus pumilus*- and *Bacillus pumilus*(Fe−)-derived carbon materials. **c** Differences in H_2O_2 selectivity between the *Bacillus pumilus*- and *Bacillus pumilus*(Fe−)-derived carbon materials. **d** Differences ORR potential between the *Bacillus pumilus*- and *Bacillus pumilus*(Fe−)-derived carbon materials. During the electrochemical measurements, 85% iR compensation was applied.

material. Both catalysts underwent identical pyrolysis processes, leading to comparable levels of N and O doping and pore structures, as shown in Supplementary Figs. 17, 18. However, they presented distinct metal contents, consistent with the differences in the contents of microbial precursors, as depicted in Fig. 2b and Supplementary Fig. 16. Compared with the *Bacillus pumilus*-derived carbon material, *Bacillus pumilus*(Fe−)-derived carbon material resulted in a 53.7% decrease in the Fe content and a 147% increase in the Mn content. Additionally, the Mg content remained nearly unchanged, with only a marginal increase of 0.5%. This observation further corroborates that during pyrolysis, Mg tends to segregate and form MgO nanocrystallites, leading to its separation from the carbon matrix[39]. After assessing the corresponding difference in catalytic performance, the *Bacillus pumilus*(Fe−)-derived carbon material exhibited a maximum decrease in H_2O_2 selectivity to 59.0% at 0 V *vs.* RHE and a negative shift in the half-wave potential to 0.55 V *vs.* RHE, as presented in Fig. 2c, d and Supplementary Fig. 19. This drastic contrast illustrates that the increase of Mg does not contribute to the ORR catalytic performance. Despite the low Fe content of 0.05 wt%, the active iron sites significantly enhances H_2O_2 selectivity, resulting in a relate increase of at least 26%. This difference in catalytic behaviour underscores the crucial role of active Fe sites, which are pyrolytically transformed from Fe-dependent proteins, in catalysing the $2e^-$ ORR.

Synthesis and characterization of catalysts featuring $FeN_{5-x}O_x$ and FeN_4 sites

During the pyrolysis of microbial cells to produce a porous carbon support, the atomic iron centres within the proteins are also modified to generate various atomic Fe sites. Further investigation is needed to understand the impact of their distinct coordination configurations on the performance of H_2O_2 electrosynthesis. *Bacillus pumilus*-derived carbon materials prepared through various thermal conversion processes were examined as examples, with a focus on their three-phase catalytic interfaces and the configurations of the trace Fe sites.

Prior to pyrolysis, the *Bacillus pumilus* cells, as shown in Fig. 3a, b and Supplementary Fig. 15, were approximately rods measuring 1–2 μm in length and 0.5 μm in diameter. After pyrolysis at temperatures ranging from 450 °C to 900 °C, the morphology of *Bacillus pumilus* cells changed significantly, condensing into porous carbon structures. The resulting *Bacillus pumilus*-derived carbon materials consisted of three-dimensional amorphous carbon with multilevel pore distributions. Scanning transmission electron microscopy images of the *Bacillus pumilus*-derived carbon material obtained at 600 °C are shown in Fig. 3c, d and Supplementary Fig. 13, whereas images obtained at 450 °C, 500 °C, 700 °C and 900 °C are provided in Supplementary Figs. 20–23. The pyrolysis temperature affected both the pore structure and the graphitic structure of the *Bacillus pumilus*-derived carbon materials. As the pyrolysis temperature increased, the specific surface area gradually increased from 31.7 $m^2 g^{-1}$ to 459.9 $m^2 g^{-1}$, accompanied by an increase in the distribution of micropores, as shown in Supplementary Fig. 24, Supplementary Table 1, and Fig. 3e. Moreover, the number of sp^3-hybridized carbons in *Bacillus pumilus*-derived carbon materials increased as the intensity ratio of the D peak (I_D, ~1400 cm^{-1}) to the G peak (I_G, ~1600 cm^{-1}) in the Raman spectra increased[40], as shown in Fig. 3f. The presence of multilevel pores and abundant carbon defects in *Bacillus pumilus*-derived carbon materials helped overcome the limitations associated with the mass diffusion of reactants and products during the ORR[41,42].

In addition to their structural advantages as carriers for ORR catalysis, the catalytic performance of *Bacillus pumilus*-derived carbon materials fundamentally depends on the intrinsic catalytic activity of the various catalytic sites present. Trace $FeN_{5-x}O_x$ sites and N/O doping sites synergistically contribute to the ORR catalytic performance, and their configurations are significantly affected by the pyrolysis temperature. The compositional changes in O and N in *Bacillus pumilus*-derived carbon materials were analysed and quantified via X-ray photoelectron spectrometer (XPS) and an elemental analyser, as depicted in Supplementary Figs. 25–26 and Fig. 3g. During the pyrolysis process, unstable organic structures are destroyed at different temperatures and undergo a series of reactions, including decomposition, reconstruction, dehydrogenation, dehydration, condensation, polymerization, oxidation, and gasification. The types of oxygen and nitrogen

https://doi.org/10.1038/s41467-024-55041-z

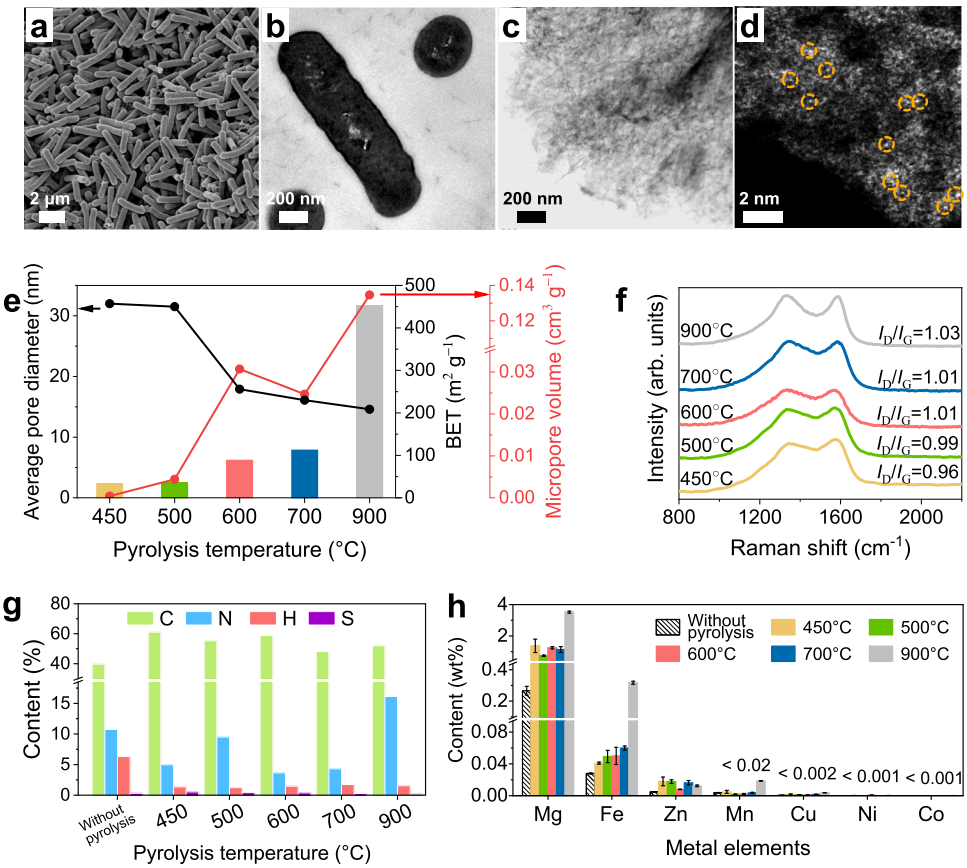

Fig. 3 | Characterization of catalysts featuring trace Fe sites. a SEM image of *Bacillus pumilus* cells prior to pyrolysis. **b** TEM image of a biological slice from *Bacillus pumilus* cells before pyrolysis, showing various cross-sections of the cells. **c** Spherical aberration-corrected scanning transmission electron microscopy (STEM) image of a *Bacillus pumilus*-derived carbon material pyrolysed at 600 °C. **d** Spherical aberration-corrected high-angle annular dark field-scanning transmission electron microscopy (HAADF-STEM) image of a *Bacillus pumilus*-derived carbon material pyrolysed at 600 °C. **e** BET surface area and pore distribution of *Bacillus pumilus*-derived carbon materials pyrolysed at different temperatures. **f** Raman spectra of *Bacillus pumilus*-derived carbon materials pyrolysed at different temperatures. **g** Analysis of the nitrogen and oxygen contents of *Bacillus pumilus*-derived carbon materials pyrolysed at different temperatures. **h** Metal content of *Bacillus pumilus*-derived carbon materials pyrolysed at different temperatures, as measured by ICP–MS. Error bars represent the standard deviation for three separate measurements.

species progressively change with different pyrolysis temperatures[43,44]. Notably, the surfaces of these catalysts retained a significant amount of oxygen, resulting from the abundant oxygenated structures in microorganisms. The atomic ratio of O decreased from 19.02% to 11.35% as the temperature increased, primarily featuring C=O and O–C–O doping within the carbon layer. However, the stability of different nitrogen species varied significantly across temperature ranges, leading to more complex compositional changes[45]. The protein-bound nitrogen in microorganisms was initially destroyed, resulting in the formation of various nitrogen-containing products after dehydration and cleavage. The unstable nitrogen-containing products underwent secondary cracking at 500–700 °C, resulting in a significant decrease in the nitrogen content from 9.50% to 3.64%, followed by a slight increase to 4.31%. The stable nitrogen species in the catalysts were ultimately retained, primarily pyrrole nitrogen, pyridine nitrogen and graphite nitrogen. Among these species, the doping of oxygen and pyrrole nitrogen on carbon supports is crucial for the formation of heterogeneous catalytic sites and enhances their ORR performance for H_2O_2 production[46–49].

In addition, metal elements—primarily Mg, Mn, Fe, Zn, Cu, Ni, and Co—were enriched in *Bacillus pumilus*-derived carbon materials. The content of Fe ranged from 0.04 wt% to 0.06 wt% in the temperature range of 450–700 °C and reached 0.32 wt% at 900 °C, as shown in Fig. 3h. This concentration was significantly lower than the typical content of active metals in SACs, which is approximately 1 wt%. Furthermore, no iron-containing crystalline structures were observed in *Bacillus pumilus*-derived carbon materials, as indicated by the XRD pattern in Supplementary Fig. 27. As shown in the spherical aberration-corrected high-angle annular dark field image in Fig. 3d, the trace metal atoms appeared as bright spots because their atomic mass was greater than that of N, O and C, as indicated by the yellow circles. The metal centres from the proteins remained atomically dispersed after pyrolysis, eliminating the need for any acid-leaching treatment. The combination of the low metal content, spatial confinement provided by protein ligands, and the amorphous porous carbon structure from microbe-derived carbon materials prevents the formation of agglomerations through sintering[50,51].

The coordination configurations of the trace Fe sites were elucidated using Fe K-edge X-ray absorption spectroscopy. The X-ray absorption near-edge structure (XANES) spectra of Fe are shown in Fig. 4a, b, with iron phthalocyanine (FePc), Fe_3O_4 and Fe_2O_3 serving as references. The valence state of the Fe species observed at 450 °C was approximately Fe(III). When the pyrolysis temperature increased to 500 °C, the Fe species were oxidized to Fe(III), and the XANES absorption edge overlapped with that of Fe_2O_3. The Fe species in the *Bacillus pumilus*-derived carbon material observed at 600 °C comprised a mixture of Fe(II) and Fe(III), similar to Fe_3O_4. As the pyrolysis temperature further increased, the Fe species were reduced to Fe(II), and the corresponding absorption edges shifted towards lower energies. The changes in the Fe valence state originate from various factors

https://doi.org/10.1038/s41467-024-55041-z

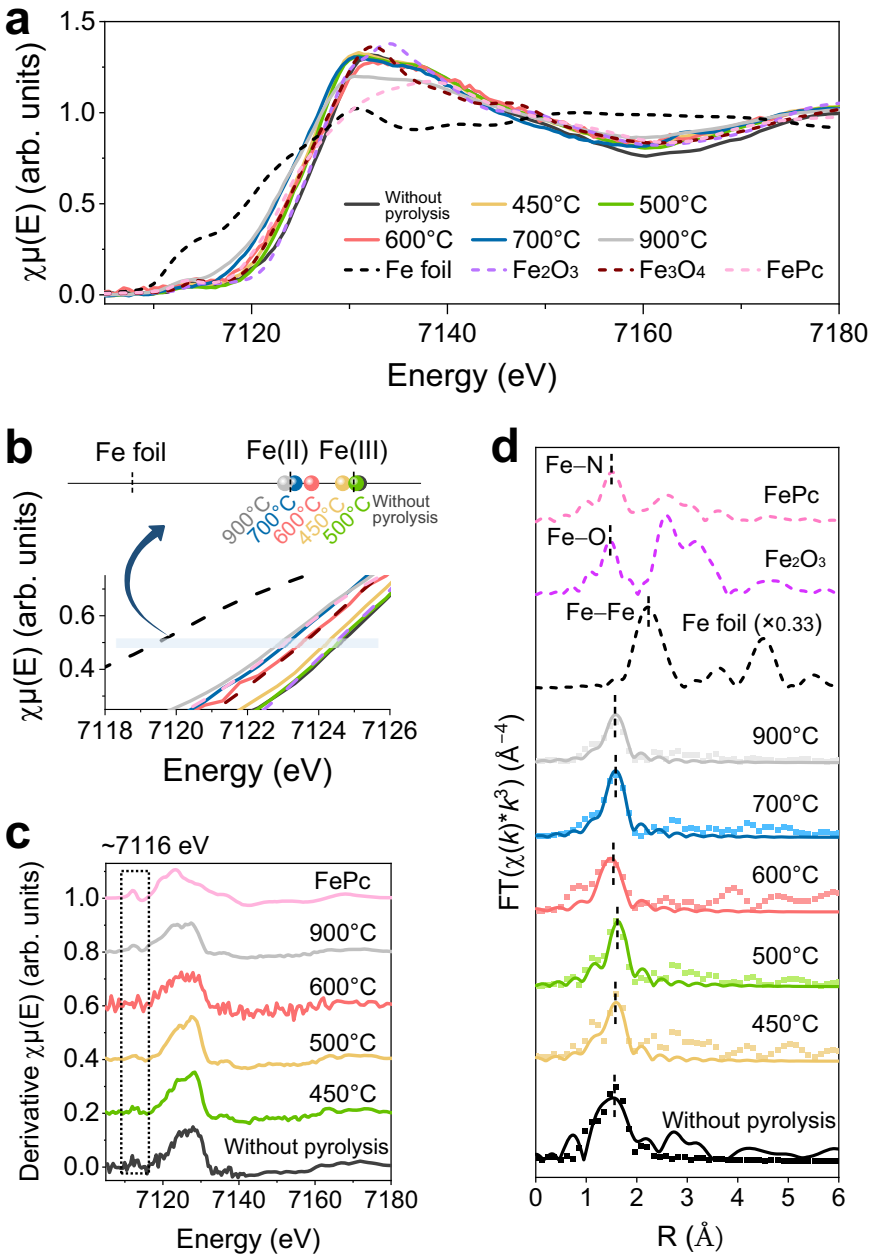

Fig. 4 | Coordination analysis of Fe sites obtained at different pyrolysis temperatures. a Normalized Fe K-edge XANES spectra of *Bacillus pumilus*-derived carbon materials. **b** The magnified corresponding near-edge region of Fe K-edge XANES spectra. **c** First derivative of the normalized Fe K-edge X-ray absorption spectra. **d** Fe K-edge EXAFS (points) and curve fit (lines) for Fe species in *Bacillus pumilus*-derived carbon materials shown in k^3-weighted *R*-space after Fourier transformation; the data are not phase corrected.

and are potentially influenced by the coordination structure of Fe single-atom sites[52,53]. The peak intensities of the Fe species pyrolysed at 450–700 °C were lower for the in-plane FeN_4 structure than those of the Fe species pyrolysed at 900 °C and FePc at ~7116 eV, indicative of a diminution in the $1s–4p_z$ shake-down transition characteristic of a square-planar configuration with high D_{4h} symmetry[54–56]. This phenomenon can be attributed to the breaking of the symmetric in-plane $Fe–N_4$ structure caused by axial coordination[57,58]. This property is more evident in the first derivative of the normalized XANES signals displayed in Fig. 4c, which are outlined with dashed boxes. The extended X-ray absorption fine structure (EXAFS) spectra of the Fe species, weighted by k^3 and obtained after Fourier transformation from R-space data, are plotted as points in Fig. 4d. The spectra of the Fe species in *Bacillus pumilus*-derived carbon materials exhibited a prominent peak at ~1.6 Å (without phase correction in this study), which was assigned to Fe–N or Fe–O coordination[59]. The characteristic absorption peak of the Fe–Fe bond, typically located at 2.17 Å relative to the Fe foil, was not observed in the spectra of the Fe species in *Bacillus pumilus*-derived carbon materials. Therefore, we inferred that these Fe atoms were coordinated with N or O atoms, differing from adjacent N/O coordination conditions.

The motifs of the Fe species were further analysed by matching the paths of Fe–N or Fe–O, and the corresponding fitting results are displayed as curve fits in Fig. 4d and Supplementary Figs. 28–30. The Fe atoms pyrolysed at 450–700 °C were coordinated with approximately five O or N atoms, labelled '$FeN_{5-x}O_x$'. The adjacent

coordination environments are proposed to be $FeNO_4$, FeN_2O_3, and FeN_3O_2, as observed at 450 °C, 500 °C and 600 °C, respectively. When the temperature was 700 °C, the Fe sites were a mixture of FeN_3O_2 and FeN_4O. For convenience, the Fe sites observed at 700 °C are referred to as FeN_4O throughout the text. At 900 °C, the coordination number of the Fe atoms was approximately four, and the motifs were presumed to be FeN_4 motifs. The corresponding fitting parameters of the $FeN_{5-x}O_x$ and FeN_4 sites are provided in Supplementary Table 3. Combining the analysis of the XANES results with DFT optimization, the predicted structural models are shown in Supplementary Fig. 31. The $FeN_{5-x}O_x$ sites were composed of a $FeN_{4-x}O_x$ ($1 \le x \le 3$) plane and an axial O ligand[54,60], with the Fe atom slightly pulled out of the $FeN_{4-x}O_x$ plane. During pyrolysis, the carbon layer surrounding the $FeN_{5-x}O_x$ sites shrank and curled. The Fe–O bonds in the $FeN_{5-x}O_x$ site broke down under heat. Then, the Fe atoms gradually bonded to the N atoms, and the $FeN_{5-x}O_x$ configuration tended to be stable[61]. Upon reaching a pyrolysis temperature of 900 °C, the Fe atoms lost their axial O coordination and transformed into FeN_4 planar structures[55]. As shown in Supplementary Fig. 31, at the $FeN_{5-x}O_x$ and FeN_4 sites, the degree of adjacent O coordination to Fe atoms was dynamically influenced by changes in the pyrolysis temperature.

Electrochemical ORR performance of catalysts featuring $FeN_{5-x}O_x$ sites

For convenience, the catalysts are labelled according to their featured Fe sites in *Bacillus pumilus*-derived carbon materials. The catalytic performance of these materials for the ORR was tested using a rotating ring-disk electrode, as shown in Supplementary Fig. 32, and the measured currents are summarized in the corresponding polarization curves in Fig. 5a. The $FeN_{5-x}O_x$ catalysts tended to catalyse the ORR via the $2e^-$ pathway, favouring H_2O_2 production, in sharp contrast to the FeN_4 catalyst. The differences in catalytic performance were evident in the calculated results for the electron transfer number and H_2O_2 selectivity, as shown in Fig. 5b. In a basic electrolyte, the FeN_3O_2

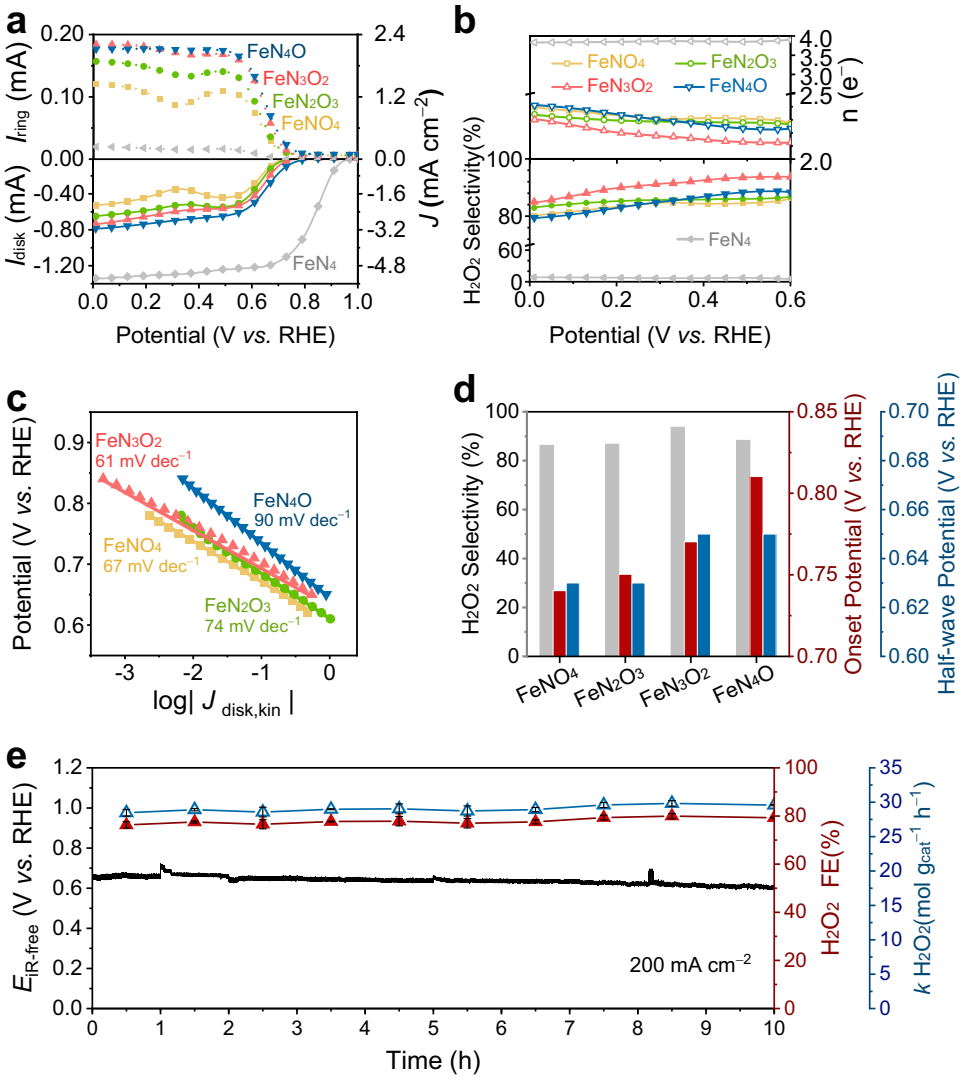

Fig. 5 | ORR electrochemical performance of catalysts featuring $FeN_{5-x}O_x$ sites. **a** ORR polarization curve measured by a rotating ring-disk electrode at 1600 rpm in O_2-saturated 0.1 M KOH. The disk electrode was used to measure oxygen reduction currents (solid lines), and the platinum ring electrode was used to measure H_2O_2 oxidation currents (dashed lines). The absolute mass loading of $FeN_{5-x}O_x$ catalysts on the electrode was 0.1 mg cm^{-2}, except for that of FeN_4 catalyst, which was 0.4 mg cm^{-2}. **b** Calculated ORR electron transfer number and H_2O_2 selectivity of $FeN_{5-x}O_x$ catalysts at 0–0.6 V *vs.* RHE. **c** Tafel plots derived from linear sweep voltammetry curves. **d** Differences in H_2O_2 selectivity, the onset potential and half-wave potential in $FeN_{5-x}O_x$ catalysts. **e** Chronopotentiometry test of FeN_3O_2 catalyst at 200 mA cm^{-2} in the flow cell. The interface impedance of the flow cell was measured to be 0.4 Ω. The absolute mass loading of FeN_3O_2 catalyst on the gas-diffusion electrode remained at 0.1 mg cm^{-2}, while the electrolyte was 1 M KOH cycled at a rate of 0.01 L min^{-1} and was replaced every hour. An 85% iR compensation was applied for rotating ring-disk electrode tests, but not for flow cell tests.

catalyst exhibited an H_2O_2 selectivity of 93.7% at 0.6 V *vs.* RHE, with an onset potential of 0.77 V *vs.* RHE for H_2O_2 onset currents up to 0.1 mA cm^{-2}. In a neutral electrolyte, the FeN_3O_2 catalyst still maintained an H_2O_2 selectivity of 88.8% at 0.6 V *vs.* RHE, as shown in Supplementary Fig. 33. Moreover, the FeN_3O_2 catalyst catalysed the ORR at currents up to the diffusion-limited value most rapidly, as reflected in the kinetic result of a lower Tafel slope in Fig. 5c. The catalytic performance of the $FeN_{5-x}O_x$ catalysts was less affected by the hydrogen peroxide reduction reaction and mass loading, as shown in Supplementary Figs. 34–35. The differences in H_2O_2 selectivity, onset potential and half-wave potential for the $FeN_{5-x}O_x$ catalysts are shown in Fig. 5d. Among them, the FeN_3O_2 catalyst exhibited efficient catalytic activity.

Electrochemical H_2O_2 production was further evaluated in a flow cell using a gas-diffusion electrode to address the O_2 mass transport issue and test the system at higher current densities. The FeN_3O_2 catalyst catalysed the ORR and steadily achieved an industrially relevant current density, as shown in Supplementary Fig. 37 and Fig. 5e. However, catalyst stability, arising from micropore flooding, demetallation and carbon oxidation[62,63], remains an enormous challenge in Fe SACs. These problems were exacerbated during Fe SAC-catalysed H_2O_2 production, resulting in a steep decrease in flow cell performance at the beginning of the test. During the chronopotentiometry test, the cathode potential of the FeN_3O_2 catalyst changed at a rate of only 5 mV h^{-1}. After 10 h, the FeN_3O_2 catalyst maintained a Faradaic efficiency for H_2O_2 production of 79.3% at 200 mA cm^{-2} without any loss of catalytic performance. Moreover, the FeN_3O_2 catalyst exhibited a high rate of H_2O_2 production, up to 29.6 mol g^{-1} h^{-1}, which exceeded the previously reported values[64]. The microstructure of the FeN_3O_2 catalyst layer was favourable for oxygen transport, as it mitigated the unexpected local oxygen transport resistance[65,66]. In addition to the porous carbon support, the high yield of H_2O_2 can be attributed to the high activity of the FeN_3O_2 sites, which have a coordination structure similar to that of the Fe centre in superoxide dismutase, converting superoxide radicals into H_2O_2 at a nearly diffusion-controlled rate[30]. The multiple active sites and multilevel pores ensured consistent and reliable H_2O_2 production over an extended period, with the production of 1 L of H_2O_2 (3 wt%) requiring only 0.035 kWh of electricity. Considering its selectivity, activity, efficiency, and stability, the FeN_3O_2 catalyst can be employed as a cost-effective catalyst for the industrial electrosynthesis of H_2O_2.

DFT calculations

DFT calculations were performed to gain atomic-level insights into the mechanism and further clarify the effect of adjacent O-coordinating dopants on the ORR catalytic performance of $FeN_{5-x}O_x$ sites. In both the 4e⁻and 2e⁻catalytic pathways, the active site first activates O_2, forming the key intermediate *OOH. The binding strength of the catalytic site to *OOH determines the activity and product selectivity of the ORR. In 0.1 M KOH, where H_2O_2 deprotonates to HO_2^- at pH > 11.6, the ORR catalytic process of $FeN_{5-x}O_x$ sites via the 2e⁻pathway can be divided into two steps as follows:

$$*O_2 + H_2O + e^- \rightarrow *OOH + OH^- \quad (1)$$

$$*OOH + e^- \rightarrow * + HO_2^- \quad (2)$$

Before constructing the computational model, we determined the catalytic sites by performing potassium thiocyanate poisoning experiments[67]. After the Fe atoms were complexed with cyanate, the ORR catalytic currents of $FeN_{5-x}O_x$ remained almost unaffected (Supplementary Fig. 39). The catalytic sites of $FeN_{5-x}O_x$ motif were hypothesized to be the C atom adjacent to the axial O[68,69], labelled the 'O-adjacent C atom', rather than the Fe atom. For comparison, the N-adjacent C atom was chosen as the catalytic site in the calculations for the FeN_4 motif. Sketches of the structural models and catalytic sites of FeN_3O_2, FeN_4O, FeN_4, and metal-free oxygen-doped carbon (labelled 'O/C') are shown in Supplementary Figs. 40–44. Using *OOH as the intermediate in the reaction of O_2 to H_2O_2, volcano plots for FeN_3O_2, FeN_4O, FeN_4, and the O/C site were constructed based on the Gibbs free energy of *OOH adsorption (ΔG_{*OOH}) and the thermodynamic ultimate potential (U_L), as shown in Fig. 6a. The volcano plot of the ideal 2e⁻pathway was located at the apex (ΔG_{*OOH} = 4.2 eV), where the experimental equilibrium potential for H_2O_2 formation was 0.68 V *vs.* RHE, with no further potential correction for *p*H-dependent product changes in this work.

The FeN_3O_2 site exhibited a ΔG_{*OOH} peak at 4.16 eV, close to the volcano plot apex, indicating impressive activity for the 2e⁻ ORR pathway. In contrast, the FeN_4 site exhibited significantly weak *OOH adsorption and had a U_L of less than 0.3 V, indicating that its N-adjacent-C site was inactive in the ORR. The reactive site in FeN_4 was found to be the iron atom, which tended to bind strongly to *OOH and cleave the O–O bond, leading to the production of H_2O via the 4e⁻ pathway. Doping of the O atom, an electron-withdrawing group, into the $FeN_{5-x}O_x$ sites, induced more electron depletion from the Fe atoms[64,70,71]. In the FeN_3O_2 motif (Supplementary Figs. 45–46), the valence electron of the Fe atom decreased by 1.07|e|, whereas that of the O-adjacent C atom increased by 0.19 |e|. This modulation of the charge distribution was achieved through O bridging between the Fe and C atoms, primarily through the axial O. As a result, *OOH was induced to bind the O-adjacent C atom in the $FeN_{5-x}O_x$ sites[72], adjusting the ΔG_{*OOH} to the optimal value for the 2e⁻ pathway, as depicted in Fig. 6b. The migration of the catalytic site from the Fe atom to the O-adjacent C atom was essential for shifting the ORR catalytic pathway[68,69,73]. This migration phenomenon has also been observed in four-coordinate Fe SACs[73] and Co SACs[69], which are labelled in black in Fig. 6a. Proper doping of adjacent O coordination sites in planar $FeN_{4-x}O_x$ ($1 \le x \le 3$) and $CoN_{4-x}O$ ($1 \le x \le 3$) sites improved the ORR performance for H_2O_2 production. Compared with the FeN_2O_2 site, the FeN_3O_2 site utilized axial O ligand coordination and exhibited better catalytic activity for the 2e⁻ ORR pathway. The uneven distribution of the electronic structure at the FeN_3O_2 site substantially enhanced the electrocatalytic performance of the Fe SACs[74,75].

The processes of $*O_2$ protonation and *OOH desorption were analysed to further elucidate the high selectivity of the $FeN_{5-x}O_x$ sites towards H_2O_2. Catalysed by the FeN_3O_2 site, the desorption process was the rate-limiting step (equation (2)) during the 2e⁻ ORR pathway, consistent with the low Tafel slope observed in Fig. 5c and the discussion in Fig. 6a, b. The transition state energy for *OOH desorption was calculated, and the results are depicted in the reaction coordinates of Fig. 6c. FeN_3O_2 site exhibited a low catalytic energy barrier of 0.35 eV for *OOH desorption to HO_2^-, which was lower than the barriers of 0.53 eV and 0.64 eV observed for FeN_4O and FeN_4 site, respectively. The lower catalytic energy barrier of $FeN_{5-x}O_x$ sites preserved the O–O bonds, thereby facilitating the desorption of *OOH[76]. Moreover, the strong binding affinity between the reactive sites and *OOH was reflected by the large number of electrons transferred during bonding. As shown in Fig. 6d, the charge state of the O-adjacent C atom in FeN_3O_2 site increased by 0.29 |e|. The charge states of the O-adjacent C atom in FeN_4O site and the N-adjacent C atom in FeN_4 site increased by 0.24 |e| and 0.10 |e|, respectively. Charge donation from the C atom to *OOH increased through O bridging, enhancing the binding strength between the C atom and *OOH. In summary, the adjacent O-coordinated dopant of FeN_3O_2 site enhanced its overall catalytic performance, promoting the efficient binding of the O-adjacent C atom to *OOH and catalysing its desorption with lower energy barriers.

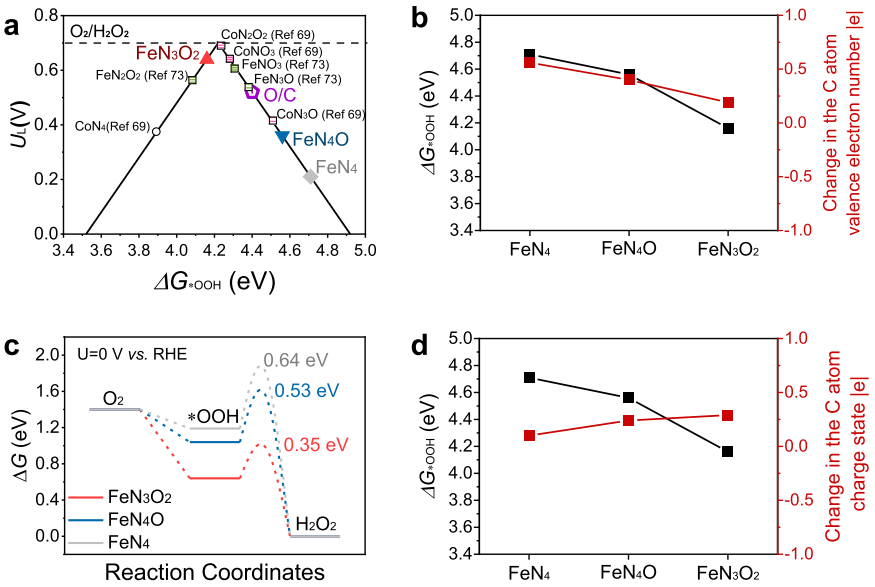

Fig. 6 | Elucidation of the mechanism of efficient ORR catalysis by the $FeN_{5-x}O_x$ sites for H_2O_2 production. a Volcano plots of the computed activity of electrochemical H_2O_2 production via the $2e^-$ ORR. The horizontal dash line indicates the equilibrium potential of O_2/H_2O_2. Except for the FeN_3O_2, FeN_4O, FeN_4, and O/C sites, the sites labelled in black were adapted from the references. **b** Calculated *OOH adsorption energies and charges of the valence electron number of the C atom in the FeN_3O_2, FeN_4O, and FeN_4 sites. **c** Free energy diagram for the $2e^-$ ORR of the FeN_3O_2, FeN_4O, and FeN_4 sites. The annotation values represent the computed kinetic barriers for *OOH to H_2O_2. **d** Calculated *OOH adsorption energies and changes in the C atom charge state at the FeN_3O_2, FeN_4O, and FeN_4 sites.

Discussion

The FeN_3O_2 catalyst, as a representative of $FeN_{5-x}O_x$ catalysts, demonstrates notable performance for H_2O_2 electrosynthesis; it achieves a high H_2O_2 selectivity of 93.7% and a remarkable yield of 29.6 mol g^{-1} h^{-1} at 200 mA cm^{-2} in a flow cell. These findings indicate that precisely regulating heteroatomic ligands within microbial Fe-dependent proteins is a sustainable, cost-effective approach for the production of Fe SACs. Adjacent O coordination modulates the charge distribution of $FeN_{5-x}O_x$ sites, causing the reactive sites to migrate from Fe atoms to O-adjacent C atoms. When catalysed by FeN_3O_2 sites, the O-adjacent C atom effectively binds the intermediate *OOH, enabling notable H_2O_2 production. In addition to adjacent O coordination, the axial O ligands in the diverse coordinated configurations of $FeN_{5-x}O_x$ sites provide steric hindrance, preventing excessive binding of *OOH to Fe atoms and thereby enhancing the ORR performance for H_2O_2 production. This research elucidates the influence of trace dopants, particularly metal elements, on biomass-derived carbon materials. By employing a rational design for the coordinated configurations of atomically active metal sites, highly active sites can enhance the catalytic performance of biomass-derived carbon materials under milder conditions. Moreover, this approach reduces the risks associated with accidents and eliminates the need for hazardous chemicals.

Methods

Chemicals and materials

Tryptone, yeast extract and beef extract (desiccant) were of FMB grade and were purchased from Sangon Biotech Co., Ltd. (Shanghai, China). Sodium chloride (NaCl), glucose, potassium dihydrogen phosphate, dipotassium hydrogen phosphate, potassium ferricyanide, diammonium citrate, sodium acetate, magnesium sulphate, manganese(II) chloride, polysorbate-80, ammonium sulphate, potassium chloride, tri(hydroxymethyl) amino methane hydrochloride (*p*H 7.5), calcium chloride, manganese sulphate, glutamate, potassium titanium oxide oxalate dehydrate ($C_4K_2O_9Ti{\cdot}2H_2O$), urea, and isopropyl alcohol (99.9%), all of analytical grade, were purchased from Sinopharm Chemical Reagent Co., Ltd (Beijing, China). Potassium hydroxide (KOH, >95%), of excellent grade, was purchased from Sinopharm Chemical Reagent Co., Ltd (Beijing, China). Nafion solution (D520) at a concentration of 5 wt% was purchased from DuPont de Nemours, Inc (USA). All reagents were used without further purification. Ultrapure water (18.2 MΩ cm^{-1}) generated with a Milli-Q system (Nihon Millipore Ltd., Japan) was used throughout the experiment. The culture conditions for *Bacillus pumilus* (No. 17816, China General Microbiological Culture Collection Center), *Bacillus pumilus*(Fe−) and other microorganisms are provided in Supplementary Table 1. Live cells were collected by centrifugation at 3500 × *g* for 10 min (Centrifuge 4530, Eppendorf, Germany). The collected cells were resuspended in a NaCl solution (0.09 wt%) three times to remove the residual medium on the cell surface. The cell pellets were freeze-dried to obtain the dried bacterial powder.

Synthesis of the ORR electrocatalysts

ORR electrocatalysts were synthesized by pyrolysing microbial cells at various temperatures. The pyrolysis precursor consisted of dried bacterial powder and urea that were mixed by milling in an agate mortar. The precursor dosages and pyrolysis temperatures used are shown in Table 1. The addition of urea improved the degree of nitrogen doping in the electrocatalysts. The tube furnace (SKGL-1200, Shanghai Jvjing Precision Instrument Manufacturing Co., Ltd., China) was programmed with a temperature ramp of 3 °C min^{-1} and maintained at the target temperature for 60 min in an argon atmosphere. After natural cooling, the carbon materials were collected and used as electrocatalysts.

Characterization of electrocatalysts

The morphology of the electrocatalysts was examined using a field-emission scanning electron microscope (s4800, Hitachi, Japan) and a transmission electron microscope (Talos F200i S/TEM, Thermo Fisher, USA). Metal atoms were captured using an aberration-corrected TEM (Titan G2 Cube 60–300 kV, Thermo Fisher, USA) operating at an accelerating voltage of 200 kV. Energy-dispersive

Table 1 | Pyrolysis precursors and temperatures for electrocatalyst synthesis

Sample	Pyrolysis temperature (°C)	Bacteria dry powder to urea ratio (g:g)
$FeNO_4$	450	0.1: 0.4
FeN_2O_3	500	0.1: 0.4
FeN_3O_2	600	0.1: 0.5
FeN_4O	700	0.1: 0.5
FeN_4	900	0.1: 0.5
$FeN_{5-x}O_x$(Fe−)	600	0.1: 0.5

X-ray (EDX) spectroscopy was performed using an Oxford IE250 system (Oxford Instruments, UK). An X-ray photoelectron spectrometer (Axis Supra, Shimadzu, Japan) was used to determine the surface composition of the electrocatalysts. The X-ray diffraction (XRD) analysis was performed using an X'Pert Pro diffractometer (PANalytical, the Netherlands) to characterize the electrocatalysts. Microporous physical and chemical adsorption measurements were conducted using an ASAP 2020 M + C instrument (Micromeritics, USA). Raman spectra were recorded with a laser confocal Raman spectrometer (LabRAM, Horiba Jobin Yvon S.A.S.) using a 532 nm laser source. The elemental composition of C, N, and O in each sample was determined using an elemental analyser (Vario EL cube, Elementar, Germany). Concurrently, the concentrations of major metal content were quantified via inductively coupled plasma–mass spectrometer (ICP–MS 7700, Agilent, USA).

X-ray absorption spectroscopy (XAS) experiments were conducted at the iron K-edge (7112 eV) using the 1W1B-XAFS beamline at the Beijing Synchrotron Radiation Facility with a double-crystal monochromator. $FeN_{5-x}O_x$ and FeN_4 data were acquired in fluorescence mode by a Lytle detector at room temperature, while reference data were collected in transmission mode. Each sample was mixed with a binder of polyvinylidene fluoride and crushed into a disk (13 mm diameter, ~1 mm thick). The E_0 value of XANES was corrected via energy calibration of the Fe foil.

X-ray absorption spectra were analysed using the Demeter software package[77]. The 3-power weighted χ(k) data were Fourier transformed after applying a K window function (Δk = 3.5–12.1). During the fitting procedure, only the adjacent coordination shell was fitted. The coordination numbers (CNs), interatomic distances (*Reff*), and edge-energy shifts (ΔE_0) were obtained by nonlinear fitting, with least-squares refinement, of the EXAFS equation to the Fourier-transformed data in R-space. The amplitude reduction factor (S_0^2) was set to 0.916, which was based on the value fitted from the spectra of the Fe foil. The Debye–Waller factor (σ^2) was fixed, and a single ΔE_0 value was applied uniformly for each sample.

Electrochemical measurements

The assessment of the $FeN_{5-x}O_x$ catalysts' catalytic performance for the ORR was evaluated in a custom three-electrode cell setup, as illustrated in Supplementary Fig. 36, utilizing a commercial bipotentiostat device (CHI 760E, Shanghai) under ambient conditions (25 °C and atmospheric pressure). A rotating ring-disk electrode (RRDE) from PINE Research Instrumentation was served as the working electrode. The disk electrode consisted of a glassy carbon disk with a geometric area of 0.2475 cm^2 (diameter = 5.61 mm), and the associated platinum ring electrode featured inner and external diameters of 6.25 mm and 7.92 mm, respectively. The collection number (*N*) of the RRDE was calibrated to 34.1% using a potassium ferricyanide solution, as detailed in Supplementary Fig. 1. A graphite rod functioned as the counter electrode, while le the reference electrode was selected based on the electrolyte, either a Hg|HgO electrode in 0.1 M KOH solution (pH = 13 ± 0.1) or a saturated calomel electrode in 0.1 M PBS solution (pH = 7.2 ± 0.1). The electrolytes were prepared in advance of the electrochemical tests, with a continuous flow of N_2 or O_2 flow to achieve N_2- or O_2-saturated solutions.

For the RRDE, the catalyst ink was formulated by dispersing 5 mg of catalyst powder into a solution comprising 800 µL of isopropanol, 170 µL of water, and 30 µL of Nafion. The mixture underwent ultrasonication for over an hour to ensure uniform dispersion and was then applied to prepare the working electrode. Either 5 or 20 µL of the catalyst ink was drop-coated onto the disk electrode to achieve mass loading of 0.1 or 0.4 mg cm^{-2}, respectively. The electrode was subsequently dehydrated under an infra-red heat source, ready for subsequent electrochemical analysis.

The H_2O_2 productivity and durability of the FeN_3O_2 catalyst were assessed in a flow-through cell, with the schematic representation provided in Supplementary Fig. 36. The tests were also monitored using a CHI 760e electrochemical workstation with a C211035 current amplifier under room temperature (20 °C) and pressure. A gas diffusion electrode (2 cm^2 in area, YSL-30T, Sinerosz Co., Ltd.), nickel foam (3 cm^2 in area and 0.1 mm thick, 99.95% purity), and an Ag/AgCl electrode functioned as the cathode, anode, and reference electrode, respectively. The anolyte and catholyte were both 1 M KOH (50 mL each, with a *p*H of 14 ± 0.1), segregated by an anion exchange membrane (4.2 cm^2 in area, Fumasep FAB-PK-130, Sinerosz Co., Ltd.). The electrolyte flow rate through the chambers was set at 10 mL min^{-1}. Oxygen was passed through the cathodic microporous layer in the gas channel at a flow rate of 50 mL min^{-1}. The anion exchange membrane was pre-treated by soaking in a 1 M KOH solution at 60 °C for 3 hours, followed by storage at room temperature for 24 h. To ensure a leak-proof setup, silicone gaskets were employed to seal the cell. The working area of the cathode and anode was 1 cm^2, and the interface impedance of the flow cell was measured to be 0.4 Ω.

For the gas diffusion electrode, the catalyst ink was prepared by mixing 5 mg of catalyst powder with the solution of 4 mL isopropanol and 1 mL water, sonicated for 1 h to ensure homogeneity. Nafion (100 µL) was then incorporated into the mixture, maintaining a 1:1 weight ratio between the ionomer and the catalyst. After stirring for 12 hours, the catalyst ink was drop-coated onto the cathodic microporous layer, with a catalyst loading of 0.1 mg cm^{-2}. The coated gas diffusion electrode was air-dried before being immersed in a 1 M KOH solution for 24 hours. Throughout this soaking process, the H^+-form Nafion was exchanged to the K^+-form Nafion, preventing acid–base reactions between H^+-form Nafion and OH^- during the ORR process.

The tested electrode potentials refer to the reversible hydrogen electrode (RHE) according to Equation (3):

$$E_{RHE} = E_{reference\ electrode} + 0.0591 \times pH + \Delta E \quad (3)$$

ΔE represents the difference in potential between the reference electrode and the RHE. The reference electrode was calibrated to a RHE in the same electrolyte before each test. For the Hg|HgO, saturated calomel and Ag|AgCl reference electrodes, the values of ΔE were 0.098 V, 0.241 V and 0.197 V, respectively.

ORR polarization curves of RRDE were recorded using linear sweep voltammetry, ranging from 0 to 1.0 V *vs.* RHE at 1600 r.p.m. and a scan rate of 10 mV s^{-1}. The measured data were adjusted to account for solution ohmic losses, with the impedance spectrum resistance measured by the PINE system and automatically compensated by 85%. The current response in the O_2-saturated electrolyte was background-corrected by subtracting the current from the N_2-saturated electrolyte, which accounts for the capacitive current. Identical test parameters were maintained for both measurements. The H_2O_2 selectivity and electron transfer number were calculated using the current from disk electrode (I_{disk}) and ring electrode (I_{ring})

based on Equations (4) and (5):

$$H_2O_2(\%) = \frac{200 \times I_{ring}}{N|I_{disk}| + I_{ring}} \quad (4)$$

$$n = 4 \times \frac{|I_{disk}|}{|I_{disk}| + \frac{I_{ring}}{N}} \quad (5)$$

The Tafel slope was calculated from the Tafel equation (6) based on the kinetic current densities calculated from the Koutecky–Levich equation (7):

$$\eta = a \log J_{disk,kin} + b \quad (6)$$

$$\frac{1}{J_{disk}} = \frac{1}{J_{disk,kin}} + \frac{1}{J_{disk,lim}} \quad (7)$$

$J_{disk,kin}$ is the kinetic current density (A cm^{-2}), whereas J_{disk} is the measured disk current density, and $J_{disk,kin}$ is the diffusion-limited current density, which was obtained by assuming a disk current with no diffusion limitation at 0.2 V *vs.* RHE as the limit value.

The H_2O_2 production efficiency and stability of the FeN_3O_2 catalyst were assessed using polarization and current-time curves in a flow-through cell. Chronopotentiometry was conducted at a constant current density of 200 mA cm^{-2}, with the catalyst's stability monitored by observing potential changes over time. A holding time of 3600 s was implemented during the measurements to ensure a steady-state current density. To prevent product accumulation that could hinder the reaction, the electrolyte was refreshed periodically at consistent intervals. The concentration of H_2O_2 produced in the cathodic electrolyte was determined using a spectrophotometric titration method. Titanium(IV) sulphate displayed a maximum absorbance at 398 nm, measured with a visible spectrophotometer (GENESYS 30, Thermo Fisher). The corresponding calibration curve, which relates its absorbance to known H_2O_2 concentrations, is presented in Supplementary Fig. 38. The $TiOSO_4$ titrant was prepared by fully dissolving 0.1 M $C_4K_2O_9Ti{\cdot}2H_2O$ in 50% v/v H_2SO_4, then stored in a sealed container at room temperature. Both the standard H_2O_2 solutions and test samples underwent the same titration procedures. To ensure test accuracy, aliquots of catholyte were collected and diluted to the concentration between 3 to 12 mM. A 0.2 mL portion of diluted catholyte was mixed with 0.8 mL of titrant by vortexing. During the reaction, colourless tetravalent titanium ions were reduced by H_2O_2 to trivalent titanium ions, producing the characteristic yellow solution.

The H_2O_2 faradaic efficiency (FE_{H2O2}) and electricity consumption (kWh kg^{-1} for 3 wt% H_2O_2) were calculated using Equations (8, 9):

$$FE_{H_2O_2}(\%) = 2 \times \frac{c_{H_2O_2} V F}{Q} \quad (9)$$

$$\text{Electricity consumption} = \frac{I \int_0^t E(t)dt}{c_{H_2O_2} M_{H_2O_2} V} \quad (10)$$

where $c_{H_2O_2}$ is the concentration of produced H_2O_2 (mol L^{-1}), V is the volume of electrolyte (L), F is the Faraday constant (96485 C mol^{-1}), Q is the amount of passed charge (C), and I and E represent the applied current (A) and cell potential (V), respectively. M_{H2O2} is the molecular weight of H_2O_2 (34 g mol^{-1}).

Computational method

Density functional theory (DFT) calculations were carried out using the Vienna Ab initio Simulation Package (VASP)[78]. The projector augmented wave (PAW) method was adopted[79]. Transition states (TS) were identified through a constrained optimization approach[80]. The exchange-correlation energy was calculated with the generalized gradient approximation (GGA), based on the Perdew–Burke–Emzerhof (PBE) functional[81]. The plane-wave basis set had an energy cut-off fixed at 400 eV. Partial occupancies of Kohn–Sham orbitals were managed using the Gaussian smearing scheme with a width of 0.2 eV. A Monkhorst–Pack k-point grid of 2 × 2 × 1 was employed to sample the Brillouin zone. This grid was used for FeN_3O_2, FeN_4O, FeN_4 and O/C moieties. Self-consistent calculations used a convergence threshold of 10^{-4} eV for energy. The force convergence limit was set to 0.05 eV $Å^{-1}$.

The following free energy corrections were considered at 298 K:

$$\Delta G = \Delta E + \Delta G_{ZPE} + \Delta G_U - T\Delta S \quad (11)$$

where ΔE, ΔG_{ZPE}, ΔG_U, and ΔS refer to the DFT-calculated energy change, the correction from the zero-point energy, the correction from the inner energy, and the correction from the entropy, respectively.

The solvent effect was evaluated to account for stabilization of adsorbates through the hydrogen bonding network in water, which was computed using VASPsol. An intermediate (*OOH) stabilization energy of −0.20 eV was incorporated.

Data availability

The data that substantiate the study's findings and contribute to the assessment of the paper's conclusions can be accessed within the paper and its Supplementary Information. All other relevant data supporting the findings of this study are available from the corresponding authors upon request. Source data file has been deposited in Figshare, https://doi.org/10.6084/m9.figshare.27653034. Source data are provided with this paper.

References

1. Ciriminna, R., Albanese, L., Meneguzzo, F. & Pagliaro, M. Hydrogen peroxide: a key chemical for today's sustainable development. *ChemSusChem* **9**, 3374–3381 (2016).
2. Tang, J. et al. Selective hydrogen peroxide conversion tailored by surface, interface, and device engineering. *Joule* **5**, 1432–1461 (2021).
3. Campos-Martin, J. M., Blanco-Brieva, G. & Fierro, J. L. Hydrogen peroxide synthesis: an outlook beyond the anthraquinone process. *Angew. Chem. Int. Ed.* **45**, 6962–6984 (2006).
4. Wang, Y., Zheng, X. & Wang, D. Design concept for electrocatalysts. *Nano Res.* **15**, 1730–1752 (2022).
5. Siahrostami, S. et al. Enabling direct H_2O_2 production through rational electrocatalyst design. *Nat. Mater.* **12**, 1137–1143 (2013).
6. Jiang, Y. et al. Selective electrochemical H_2O_2 production through two-electron oxygen electrochemistry. *Adv. Energy Mater.* **8**, 1801909 (2018).
7. Gan, T. & Wang, D. Atomically dispersed materials: Ideal catalysts in atomic era. *Nano Res.* **17**, 18–38 (2023).
8. Jung, E. et al. Atomic-level tuning of Co–N–C catalyst for high-performance electrochemical H_2O_2 production. *Nat. Mater.* **19**, 436–442 (2020).
9. Chen, J. et al. Kinetically restrained oxygen reduction to hydrogen peroxide with nearly 100% selectivity. *Nat. Commun.* **13**, 2808 (2022).
10. Yu, S. et al. High activity and selectivity of single palladium atom for oxygen hydrogenation to H_2O_2. *Nat. Commun.* **13**, 4737 (2022).
11. An, Z. et al. Highly active, ultra-low loading single-atom iron catalysts for catalytic transfer hydrogenation. *Nat. Commun.* **14**, 6666 (2023).
12. Dessalle, A., Quílez-Bermejo, J., Fierro, V., Xu, F. & Celzard, A. Recent progress in the development of efficient biomass-based ORR electrocatalysts. *Carbon* **203**, 237–260 (2023).

13. Borghei, M., Lehtonen, J., Liu, L. & Rojas, O. J. Advanced biomass-derived electrocatalysts for the oxygen reduction reaction. *Adv. Mater.* **30**, 1703691 (2018).
14. Tiwari, J. N. et al. Multi-heteroatom-doped carbon from waste-yeast biomass for sustained water splitting. *Nat. Sustain.* **3**, 556–563 (2020).
15. Wang, L., Ambrosi, A. & Pumera, M. "Metal-free" catalytic oxygen reduction reaction on heteroatom-doped graphene is caused by trace metal impurities. *Angew. Chem.* **125**, 14063–14066 (2013).
16. Liu, J. et al. High-performance oxygen reduction electrocatalysts based on cheap carbon black, nitrogen, and trace iron. *Adv. Mater.* **25**, 6879–6883 (2013).
17. Pan, Y. et al. Regulating the coordination structure of single-atom Fe–N_xC_y catalytic sites for benzene oxidation. *Nat. Commun.* **10**, 4290 (2019).
18. Sun, K., Shan, H., Neumann, H., Lu, G.-P. & Beller, M. Efficient iron single-atom catalysts for selective ammoxidation of alcohols to nitriles. *Nat. Commun.* **13**, 1848 (2022).
19. Gu, H. et al. Adjacent single-atom irons boosting molecular oxygen activation on MnO_2. *Nat. Commun.* **12**, 5422 (2021).
20. Huang, L., Chen, J., Gan, L., Wang, J. & Dong, S. Single-atom nanozymes. *Sci. Adv.* **5**, eaav5490 (2019).
21. Long, X. et al. Graphitic phosphorus coordinated single Fe atoms for hydrogenative transformations. *Nat. Commun.* **11**, 4074 (2020).
22. Qin, J. et al. An enzyme-mimic single Fe–N_3 atom catalyst for the oxidative synthesis of nitriles via C–C bond cleavage strategy. *Sci. Adv.* **8**, eadd1267 (2022).
23. Li, R. & Wang, D. Understanding the structure-performance relationship of active sites at atomic scale. *Nano Res.* **15**, 6888–6923 (2022).
24. Wodrich, M. D. & Hu, X. Natural inspirations for metal–ligand cooperative catalysis. *Nat. Rev. Chem.* **2**, 0099 (2017).
25. Wang, A., Li, J. & Zhang, T. Heterogeneous single-atom catalysis. *Nat. Rev. Chem.* **2**, 65–81 (2018).
26. Huang, X. & Groves, J. T. Oxygen activation and radical transformations in heme proteins and metalloporphyrins. *Chem. Rev.* **118**, 2491–2553 (2018).
27. Bullock, R. M. et al. Using nature's blueprint to expand catalysis with Earth-abundant metals. *Science* **369**, eabc3183 (2020).
28. Whittaker, J. W. & Solomon, E. I. Spectroscopic studies on ferrous nonheme iron active sites: magnetic circular dichroism of mononuclear iron sites in superoxide dismutase and lipoxygenase. *J. Am. Chem. Soc.* **110**, 5329–5339 (1988).
29. Kitagawa, T. et al. A functional model for the cysteinate-ligated nonheme iron enzyme superoxide reductase (SOR). *J. Am. Chem. Soc.* **128**, 14448–14449 (2006).
30. Sheng, Y. et al. Superoxide dismutases and superoxide reductases. *Chem. Rev.* **114**, 3854–3918 (2014).
31. Liu, J., Wu, X., Yao, M., Xiao, W. & Zha, J. Chassis engineering for microbial production of chemicals: From natural microbes to synthetic organisms. *Curr. Opin. Biotechnol.* **66**, 105–112 (2020).
32. Yang, C. et al. Carbon dots-fed *Shewanella oneidensis* MR-1 for bioelectricity enhancement. *Nat. Commun.* **11**, 1379 (2020).
33. Han, X. et al. Mn–N_4 oxygen reduction electrocatalyst: operando investigation of active sites and high performance in zinc–air battery. *Adv. Energy Mater.* **11**, 2002753 (2021).
34. Li, J. et al. Atomically dispersed manganese catalysts for oxygen reduction in proton-exchange membrane fuel cells. *Nat. Catal.* **1**, 935–945 (2018).
35. Andrews, S. C., Robinson, A. K. & Rodríguez-Quiñones, F. Bacterial iron homeostasis. *FEMS Microbiol. Rev.* **27**, 215–237 (2003).
36. Xu, X., Liu, Y., Du, G., Ledesma-Amaro, R. & Liu, L. Microbial chassis development for natural product biosynthesis. *Trends Biotechnol.* **38**, 779–796 (2020).
37. Neilands, J. B. *Microbial Iron Metabolism: a Comprehensive Treatise*. (Academic Press, New York, 1974).
38. Puig, S., Askeland, E. & Thiele, D. J. Coordinated remodeling of cellular metabolism during iron deficiency through targeted mRNA degradation. *Cell* **120**, 99–110 (2005).
39. Li, X., Guan, B. Y., Gao, S. & Lou, X. W. D. A general dual-templating approach to biomass-derived hierarchically porous heteroatom-doped carbon materials for enhanced electrocatalytic oxygen reduction. *Energy Environ. Sci.* **12**, 648–655 (2019).
40. Kim, H. W. et al. Efficient hydrogen peroxide generation using reduced graphene oxide-based oxygen reduction electrocatalysts. *Nat. Catal.* **1**, 282–290 (2018).
41. Asset, T. & Atanassov, P. Iron–nitrogen–carbon catalysts for proton exchange membrane fuel cells. *Joule* **4**, 33–44 (2020).
42. Zhao, Z. et al. Defect engineering in carbon materials for electrochemical energy storage and catalytic conversion. *Mater. Adv.* **4**, 835–867 (2023).
43. Bagri, A. et al. Structural evolution during the reduction of chemically derived graphene oxide. *Nat. Chem.* **2**, 581–587 (2010).
44. Li, X. et al. Simultaneous nitrogen doping and reduction of graphene oxide. *J. Am. Chem. Soc.* **131**, 15939–15944 (2009).
45. Chen, W. et al. Transformation of nitrogen and evolution of N-containing species during algae pyrolysis. *Environ. Sci. Technol.* **51**, 6570–6579 (2017).
46. Lu, Z. et al. High-efficiency oxygen reduction to hydrogen peroxide catalysed by oxidized carbon materials. *Nat. Catal.* **1**, 156–162 (2018).
47. Chen, S. et al. Chemical identification of catalytically active sites on oxygen-doped carbon nanosheet to decipher the high activity for electro-synthesis hydrogen peroxide. *Angew. Chem. Int. Ed.* **60**, 16607–16614 (2021).
48. Lim, J. S. et al. Designing highly active nanoporous carbon H_2O_2 production electrocatalysts through active site identification. *Chem* **7**, 3114–3130 (2021).
49. Zhang, J., Yang, H. & Liu, B. Coordination engineering of single-atom catalysts for the oxygen reduction reaction: a review. *Adv. Energy Mater.* **11**, 2002473 (2021).
50. Hwang, J. et al. Controlling the morphology of metal–organic frameworks and porous carbon materials: metal oxides as primary architecture-directing agents. *Chem. Soc. Rev.* **49**, 3348–3422 (2020).
51. Datye, A. K., Xu, Q., Kharas, K. C. & McCarty, J. M. Particle size distributions in heterogeneous catalysts: what do they tell us about the sintering mechanism? *Catal. Today* **111**, 59–67 (2006).
52. Zhang, H. et al. Single atomic iron catalysts for oxygen reduction in acidic media: particle size control and thermal activation. *J. Am. Chem. Soc.* **139**, 14143–14149 (2017).
53. Yin, S. et al. Seizing gaseous Fe^{2+} to densify O_2-accessible Fe–N_4 sites for high-performance proton exchange membrane fuel cells. *Energy Environ. Sci.* **15**, 3033–3040 (2022).
54. Li, J. et al. Structural and mechanistic basis for the high activity of Fe–N–C catalysts toward oxygen reduction. *Energy Environ. Sci.* **9**, 2418–2432 (2016).
55. Liu, W. et al. Discriminating catalytically active FeN_x species of atomically dispersed Fe–N–C catalyst for selective oxidation of the C–H bond. *J. Am. Chem. Soc.* **139**, 10790–10798 (2017).
56. Fei, H. et al. General synthesis and definitive structural identification of MN_4C_4 single-atom catalysts with tunable electrocatalytic activities. *Nat. Catal.* **1**, 63–72 (2018).
57. Cao, R. et al. Promotion of oxygen reduction by a bio-inspired tethered iron phthalocyanine carbon nanotube-based catalyst. *Nat. Commun.* **4**, 2076 (2013).
58. Chen, K. et al. Iron phthalocyanine with coordination induced electronic localization to boost oxygen reduction reaction. *Nat. Commun.* **11**, 4173 (2020).
59. Marshall-Roth, T. et al. A pyridinic Fe–N_4 macrocycle models the active sites in Fe/N-doped carbon electrocatalysts. *Nat. Commun.* **11**, 5283 (2020).

60. Zhang, H. et al. A graphene-supported single-atom FeN_5 catalytic site for efficient electrochemical CO_2 reduction. *Angew. Chem.* **131**, 15013–15018 (2019).
61. Li, J. et al. Thermally driven structure and performance evolution of atomically dispersed FeN_4 sites for oxygen reduction. *Angew. Chem. Int. Ed.* **58**, 18971–18980 (2019).
62. Shao, Y., Dodelet, J.-P., Wu, G. & Zelenay, P. PGM-free cathode catalysts for PEM fuel cells: a mini-review on stability challenges. *Adv. Mater.* **31**, 1807615 (2019).
63. Zhao, L. et al. Materials engineering toward durable electrocatalysts for proton exchange membrane fuel cells. *Adv. Energy Mater.* **12**, 2102665 (2022).
64. Cao, P. et al. Metal single-site catalyst design for electrocatalytic production of hydrogen peroxide at industrial-relevant currents. *Nat. Commun.* **14**, 172 (2023).
65. Islam, M. N. et al. Designing fuel cell catalyst support for superior catalytic activity and low mass-transport resistance. *Nat. Commun.* **13**, 6157 (2022).
66. Wu, Z. Y. et al. A general synthesis of single atom catalysts with controllable atomic and mesoporous structures. *Nat. Synth.* **1**, 658–667 (2022).
67. Jiang, W. J. et al. Understanding the high activity of Fe–N–C electrocatalysts in oxygen reduction: Fe/Fe_3C nanoparticles boost the activity of $Fe–N_x$. *J. Am. Chem. Soc.* **138**, 3570–3578 (2016).
68. Zhu, Y. et al. Switching theoxygen reduction reaction pathway via tailoring the electronic structure of FeN_4/C catalysts. *ACS Catal.* **11**, 13020–13027 (2021).
69. Tang, C. et al. Tailoring acidic oxygen reduction selectivity on single-atom catalysts via modification of first and second coordination spheres. *J. Am. Chem. Soc.* **143**, 7819–7827 (2021).
70. Fan, W. et al. Rational design of heterogenized molecular phthalocyanine hybrid single-atom electrocatalyst towards two-electron oxygen reduction. *Nat. Commun.* **14**, 1426 (2023).
71. Lee, B.-H. et al. Supramolecular tuning of supported metal phthalocyanine catalysts for hydrogen peroxide electrosynthesis. *Nat. Catal.* **6**, 234–243 (2023).
72. Ramaswamy, N., Tylus, U., Jia, Q. & Mukerjee, S. Activity descriptor identification for oxygen reduction on nonprecious electrocatalysts: linking surface science to coordination chemistry. *J. Am. Chem. Soc.* **135**, 15443–15449 (2013).
73. Jiang, K. et al. Highly selective oxygen reduction to hydrogen peroxide on transition metal single atom coordination. *Nat. Commun.* **10**, 3997 (2019).
74. Xin, C. et al. Integration of morphology and electronic structure modulation on atomic iron–nitrogen–carbon catalysts for highly efficient oxygen reduction. *Adv. Funct. Mater.* **32**, 2108345 (2022).
75. Dai, Y. et al. Tailoring the d-orbital splitting manner of single atomic sites for enhanced oxygen reduction. *Adv. Mater.* **35**, 2210757 (2023).
76. Li, X. et al. Molecule confined isolated metal sites enable the electrocatalytic synthesis of hydrogen peroxide. *Adv. Mater.* **34**, 2104891 (2022).
77. Ravel, B. & Newville, M. ATHENA, ARTEMIS, HEPHAESTUS: data analysis for X-ray absorption spectroscopy using IFEFFIT. *J. Synchrotron Radiat.* **12**, 537–541 (2005).
78. Kresse, G. & Furthmüller, J. Efficiency of ab-initio total energy calculations for metals and semiconductors using a plane-wave basis set. *Comp. Mater. Sci.* **6**, 15–50 (1996).
79. Blöchl, P. E. Projector augmented-wave method. *Phys. Rev. B* **50**, 17953–17979 (1994).
80. Liu, Z. P. & Hu, P. General rules for predicting where a catalytic reaction should occur on metal surfaces: a density functional theory study of C–H and C–O bond breaking/making on flat, stepped, and kinked metal surfaces. *J. Am. Chem. Soc.* **125**, 1958–1967 (2003).
81. Perdew, J. P. et al. Atoms, molecules, solids, and surfaces: applications of the generalized gradient approximation for exchange and correlation. *Phys. Rev. B* **46**, 6671–6687 (1992).

Acknowledgements

This work was supported by the National Natural Science Foundation of China (grant numbers 22025603, F.Z. 22236007, F.Z. and 42021005, F.Z.). We acknowledge the support from the SSRF (beamline 11B) and BSRF (beamline 1W1B) for the allocation of synchrotron beamtime. We thank Prof. Maozi Lin of Fujian Polytechnic Normal University for providing the *Bacillus pumilus* strains.

Author contributions

X.-F.X. performed the experiments, collected and analysed the data, and composed the manuscript. Z.-C.Z. conceived the idea, designed the experiments, performed the XAFS measurements, analysed the data, and revised the manuscript. S.-H.Y. helped test the flow cell and analysed the catalytic performance. Z.-J.X. and T.G. performed the XAFS data analysis. R.-H.Y. and J.-S.W helped test and analyse the AC-STEM results. X.-C.T. helped revise the manuscript. Y.-X.J. provided the experimental instruments for the electrochemical tests. D.-S.W. and F.Z. designed the research projects and experiments, performed the integrated analyses, and revised the manuscript. All the authors commented on the manuscript and approved the final version of the manuscript.

Competing interests

The authors declare no competing interests.

Additional information

Supplementary information The online version contains supplementary material available at https://doi.org/10.1038/s41467-024-55041-z.

Correspondence and requests for materials should be addressed to Dingsheng Wang or Feng Zhao.

Peer review information *Nature Communications* thanks Shichao Ding and Xie Quan for their contribution to the peer review of this work. A peer review file is available.